Laser Powder Bed Fusion of Pure Titanium: Optimization of Processing Parameters by Means of Efficient Volumetric Energy Density Approach

metals

Article

Laser Powder Bed Fusion of Pure Titanium: Optimization of Processing Parameters by Means of Efficient Volumetric Energy Density Approach

Claudio F. Badini *, Tommaso Santero, Michele Rosito and Elisa Padovano

Department of Applied Science and Technology, Politecnico di Torino, Corso Duca degli Abruzzi 24, 10129 Turin, Italy; tommaso.santero@polito.it (T.S.); michele.rosito@polito.it (M.R.); elisa.padovano@polito.it (E.P.)
* Correspondence: claudio.badini@polito.it

Abstract: This paper focuses on optimizing the process parameters for manufacturing commercially pure titanium grade 2 using Laser Powder Bed Fusion (L-PBF) technology. The most common approach involves trial-and-error builds with varying parameter combinations, followed by characterizing the bulk samples for defects and the microstructure. This method, typically based on Volumetric Energy Density (VED), is time-consuming and overlooks key powder properties. An alternative approach involves the use of efficient Volumetric Energy Density (VED_{eff}), which represents the energy density effectively available for the L-PBF process, considering both the process parameters and powder properties such as absorptivity and thermal diffusivity. In this study, VED_{eff} was applied and compared to a work window defined by thermodynamic data, with limits corresponding to the energy needed for titanium melting and evaporation. Forty-two tests were performed with different combinations of laser powers and scanning speeds; the samples were then characterized in terms of porosity, microstructure, and hardness. The findings showed no correlation between VED and the work window while VED_{eff} aligned with the work window, although the highest relative densities (>99%) and hardness values were achieved in a narrower range. Despite this, the VED_{eff} approach proved to be a useful starting point for optimizing the process parameters.

Keywords: commercially pure titanium; Laser Powder Bed Fusion; process optimization; efficient volumetric energy density; powder absorptivity; thermal diffusivity; thermodynamic work window

check for updates

Citation: Badini, C.F.; Santero, T.; Rosito, M.; Padovano, E. Laser Powder Bed Fusion of Pure Titanium: Optimization of Processing Parameters by Means of Efficient Volumetric Energy Density Approach. *Metals* **2024**, *14*, 1357. https://doi.org/10.3390/met14121357

Academic Editor: Antonio Riveiro

Received: 29 October 2024
Revised: 21 November 2024
Accepted: 25 November 2024
Published: 28 November 2024

1. Introduction

The Laser Powder Bed Fusion (L-PBF) of metals is today a well-known additive manufacturing (AM) technique. This manufacturing process has attracted great interest from both the academic and the industrial communities thanks to the several advantages it offers over traditional manufacturing processes of metal-based components such as forging, casting, and machining. In fact, this AM technique grants benefits such as great design flexibility and, consequently, the chance to customize industrial products. In addition, it allows for both the weight reduction of the manufactured parts as well as reducing raw material consumption and waste production.

L-PBF is a one-step and a net- or near-net-shaped way of manufacturing components with complex geometries that has the merit of avoiding or limiting the need for assembling parts (for instance, by welding) and performing final tooling or surface finishing. For these reasons, L-PBF has been used in several application fields such as the automotive, aerospace, biomedical, and energy industries.

In this AM process, the final part is obtained from a CAD (Computer-Aided Design) model of the component. During the process, the component is built layer-by-layer: each layer is built after the deposition of a homogeneous powder bed that is selectively melted to form the section of the component. These steps are repeated until the complete part is obtained.

In recent years, a great number of papers dealing with the L-PBF of metal-based materials have been published. Progress in this field has been well summarized in some recent reviews [1–6]. Other reviews have focused on the state of the art for the L-PBF of specific classes of metal-based materials like steels [7–9], aluminum alloys [10], magnesium alloys [11,12], nickel alloys [13,14], titanium alloys [15–20], copper alloys [21], tungsten [22], tantalum [23], rare earth metals [24], and metal matrix composites [25–27].

This extensive literature shows that the same material can be processed under different conditions, all of which grant good final density and mechanical features. This is not surprising at all since several processing parameters affect the microstructure and properties of the metal parts produced by L-PBF. In particular, the laser power (P), the scanning speed (v), the distance between two laser passes (known as the "hatching distance" h), the thickness of each powder layer (t), and the laser spot diameter (Φ) are generally believed to have the greatest impact on the quality of the printed parts. For this reason, similar results can be obtained by using quite different combinations of these processing parameters.

It is very hard to investigate, experimentally, "in situ", the effect of each processing parameter during the printing process because of the extremely short interaction period involving the laser and the powder bed and the dramatical and rapid variation in the temperature and microstructure. For this reason, the optimization of the processing parameters is frequently obtained by adopting a trial-and-error method based on tuning the above-mentioned parameters into different steps. The density of the printed part or its residual porosity is frequently taken as an index to identify optimized parameters. The residual porosity is strictly related to the metal powder–laser interaction, in addition to the material properties, and should, in principle, be avoided because it greatly affects the microstructural integrity and the properties of the final parts.

Different kinds of defects can be observed in parts processed by L-PBF, namely a lack of fusion, a keyhole, and gas porosity [28]. An insufficient amount of delivered energy, generally caused by an insufficient laser power associated with a high scanning speed, results in irregularly shaped porosity known as a lack of fusion and located between adjacent laser tracks or at the interface between neighboring molten layers. Conversely, the delivery of too much energy could result in porosity due to the overmelting and vaporization of volatile substances with the formation of keyhole porosities. Similarly, defects can also result from gas entrapment during the raw powder atomization or chemical reactions.

According to the literature, the most widely used approach for optimizing the L-PBF process is based on changing, step by step, the energy delivered by the laser source to the unit of volume of the powder bed. This Volumetric Energy Density (VED) can be calculated as a function of some of the previously mentioned process parameters according to Equation (1):

$$VED = \frac{P}{v\,t\,h} \quad (1)$$

However, this approach fails to consider the intrinsic properties of the material printed. In fact, material absorptivity and particle size greatly affect the fraction of the energy delivered to the powder bed that can be used for the process.

In addition, also, this way for optimizing the processing parameters is time-consuming and costly. Several models aimed at simulating the complex physical phenomena occurring during the L-PBF process have been proposed [29–36] with the goal of predicting the processing parameters that reduce porosity and improve the final mechanical features. Many different theoretical approaches can be exploited. For instance, they include finite element analysis [29], machine learning [30,31], artificial neural networks [32,33], and dimensionless numbers [34–36]. All these models seem to be not very user-friendly as they require dedicated software and several input data.

A modified VED equation was proposed by Ferro et al. [37]. In contrast to the traditional VED, this equation also considers the interaction between the laser source and the powder bed to calculate the effective amount of energy (Efficient Volumetric Energy

Density, VED_{eff}) that is available for heating and melting the powder bed. To this purpose, the absorptivity of the laser radiation (β), the thermal diffusivity of the powder bed (α), and the laser spot diameter (Φ) were introduced in the VED_{eff} calculation (Equation (2)):

$$VED_{eff} = \frac{P\,\beta}{h\,\sqrt{4\,\alpha\,\Phi\,v}} \quad (2)$$

The absorptivity and thermal diffusivity of the metallic powders can be quite easily experimentally measured or taken from literature databases; the laser spot diameter is usually provided by the L-PBF provider. This equation was successfully used as a thumb rule to identify a set of processing parameters suitable for printing an almost fully dense AlSi10Mg alloy and Maraging steel 300 [37]. In fact, low residual porosity was detected when a narrow range of VED_{eff} was adopted.

The energy delivered by the laser source (VED) and the energy actually available for the fusion of a unit of volume of the powder bed (VED_{eff}) can also be compared with a work window that can be assessed by using thermodynamic data. The lower limit of the work window is the energy necessary to heat the powder to the melting temperature and then to melt it. The upper limit can be calculated by adding the vaporization heat to the energy necessary to achieve the lower limit. Very likely, the energy corresponding to the lower limit is not sufficient to ensure welding between adjacent layers. In fact, this happens only if the laser radiation penetrates inside the current molten layer and reaches the layer below. On the other hand, the upper limit should not be exceeded to avoid pore formation due to the emission of volatile substances.

In the present study, the manufacturing of pure titanium (CP-Ti) by L-PBF was investigated. The L-PBF of CP-Ti is considered to have great potential for manufacturing customized biomedical implants [19]. In fact, pure titanium is suitable for application in metallic implants owing to its biocompatibility and corrosion resistance, and the 3D printing technique allows for obtaining cellular structures. In addition, pure titanium is advantageous with respect to the Ti-6Al-4V alloy, which shows better mechanical feature instead, because of its lower toxicity.

Previous investigations on this subject suggested the adoption of quite-dissimilar values of VED since all of them were claimed to produce dense Cp-Ti parts. Optimized VED values should range between 56 J/mm^3 and 60 J/mm^3 according to Fisher et al. [38] and between 32 J/mm^3 and 47 J/mm^3 according to Depboylu et al. [39] while Zhang et al. [40] selected a VED value of 69.4 J/mm^3 and Kovaci [41] used a VED value of 26 J/mm^3. Conversely, a much higher energy density (94 J/mm^3) was also adopted for the L-PBF of Cp titanium [42] and for Ti-6Al-4V alloy (136 J/mm^3) [43]. The wide range of optimized VED values, and then of processing parameters, reported in the literature for the L-PBF processing of Ti can be ascribed to some peculiar characteristics of this metal, like its reflectivity and its tendency to be contaminated by oxygen. Reflectivity reduces the fraction of laser radiation absorbed by the powder bed, but the contamination by oxygen of the surface of titanium particles greatly improves the absorptivity of this material [44].

The present study was aimed at investigating the use of the VED or VED_{eff} equations and the work window for the prediction of L-PBF processing parameters suitable for obtaining pure titanium samples with high density. To this purpose, a high number of samples were processed by using different combinations of the processing parameters and the relevant values of volumetric energy densities were compared with the work window. The microstructure, the density, and the hardness of the samples processed under different conditions were investigated to identify the optimized parameters set and to check the effectiveness of the comparison between VED and VED_{eff} with the work window for selecting it.

2. Materials and Methods

2.1. Cp Titanium Powder Characterization

Commercially pure grade 2 titanium powder produced by gas atomization (supplied by TLS Technik GmbH, Bitterfeld, Germany) was used in this work. According to the producer datasheet, the powder contains very low amounts of impurities. The chemical composition of the powder is provided in Table 1.

Table 1. Chemical composition of CP-Ti gr. 2 powder.

Element	N	C	H	Fe	O	Ti
Content (wt.%)	0.011	0.01	0.002	0.059	0.18	Balance

The powder density was measured using a Helium pycnometer (Ultrapyc 5000, Anton Paar GmbH, Graz, Austria). The morphology and the composition of the powder particles were investigated by SEM-EDS (FE-SEM Zeiss, Oberkochen, Germany). The particle size distribution was investigated by optical microscopy with the use of ImageJ (version 1.54d) software.

Powder flowability (evaluated using the Hall method, ASTM B213-20 [45]), apparent density, and tap density were measured. Starting with these experimental values, the Hausner Ratio (HR) and the Compressibility Index (CI) were calculated. The powder reflectivity was measured in the range between 200 and 2000 nm and steps of 0.665 nm by reflectance spectroscopy (Varian Cary 5000 spectrophotometer, Agilent, Santa Clara, CA, USA), using an instrument equipped with integrating sphere and a software for the conversion of reflectance spectrum into the absorptivity one according to the Kubelka–Munk algorithm.

2.2. L-PBF Process

The L-PBF printing machine (MetalOne 250W, Sharebot, Lecco, Italy), equipped with a continuous wave fiber laser (Nd: YAG with a wavelength of 1064 nm and a spot size of 100 µm), was employed to print cubic samples of CP grade 2 titanium with dimensions of $10 \times 10 \times 12$ mm^3. These samples were manufactured in a chamber purged with argon gas; the oxygen content inside the chamber was maintained below 0.1% during the printing process. Six specimens were produced during each test, which was carried out by keeping constant the VED value and adopting a different combination of power and scanning speed for each cubic sample. The VED values adopted for each single test were selected with the aim of covering the wide range of VED reported in the literature for L-PBF of Ti and its alloys [38–43]. The different combinations of power and scanning speed were selected in such a way that they could be settled in most commercial equipment used for L-PBF.

The scanning directions were rotated by 67 between subsequent layers. Power values of 90, 100, 110, 120, 130, and 140 W, combined with scanning speeds ranging between 221 and 1667 mm/s, were used. This resulted in VED values ranging between 35 and 150 J/mm^3, corresponding to VED_{eff} values ranging between 11.19 and 31.67 J/mm^3. The hatching distance (0.08 mm) and the layer thickness (0.03 mm) were kept constant. A summary of adopted process parameters is shown in Table 2.

Table 2. Summary of adopted process parameters.

Process Parameter	Value
Laser Powers P (W)	90–100–110–120–130–140
Scanning Speeds v (mm/s)	221 ÷ 1667
Hatching Distance h (µm)	80
Layer Thickness (µm)	30
Volumetric Energy Densities VED (J/mm^3)	35 ÷ 150
Efficient VED (J/mm^3)	11.19 ÷ 31.67

After the process, the samples were removed from the platform. No thermal treatment was performed before the sample characterization.

2.3. Microstructural Characterization

The surfaces of the cubic samples manufactured by L-PBF were polished using abrasive SiC paper P400 to remove the process roughness. Subsequently, their density was measured by Archimedes' method (ASTM B311-17 [46]) and the porosity was calculated by comparing the measured density with the true density of the titanium powder, which was evaluated using a Helium pycnometer (4.52 g/cm^3). Optical microscopy and microhardness measurements, carried out on the cross-sections of the samples, were used to strengthen the outcomes of the density test. A cross-section of the samples parallel to the building direction (X-Z plane section) was obtained using a diamond wheel. The cross-sections were polished according to metallography practices (using abrasive papers and silica suspension) and observed with an optical microscope (Leica DMI 5000 M, Leica Microsystem, Wetzlar, Germany). The sample microstructure was also examined via optical microscopy after etching with Kroll's solution (samples were immersed for 15 s in a water solution containing 6% vol. of nitric acid and 3% vol. of hydrofluoric acid).

Vickers microhardness measurements were also carried out to evaluate the effect of the processing parameters on the mechanical behavior. A digital microhardness tester (HNVS-1000DX, HST Group, Jinan, China) was used for this purpose. Microhardness measurements were conducted on the X-Z cross-sections (a plane parallel to the building direction) of the specimens according to the BS EN ISO 6507-1:2023 standard [47]. The cross-section surfaces were polished, and six indentations for each sample were performed at a distance of at least 0.5 mm apart, with a load of 100 g maintained for 10 s. Even though the measurements were carried out far from the pores visible on the surface, the presence of defects and the corresponding sample density were found to affect the hardness values.

3. Results and Discussion

3.1. Characterization of Cp Titanium Powder

The Cp titanium powder showed a density of 4.52 g/cm^3. Most of the titanium particles showed a spherical shape, but some agglomerates of very small particles were also observed, and EDS highlighted that the particle surface was slightly contaminated by oxygen (Figure 1). The contamination of the particle surface was very likely due to batch storage. Figure 2 shows that the particle size distribution was rather narrow, with particle dimensions ranging between 3 and 51 µm. The particle size distribution was not symmetrical as particles with sizes in the range between 12 and 17 µm represented the most important fraction of the powder while half of the particles showed sizes above 21.30 µm.

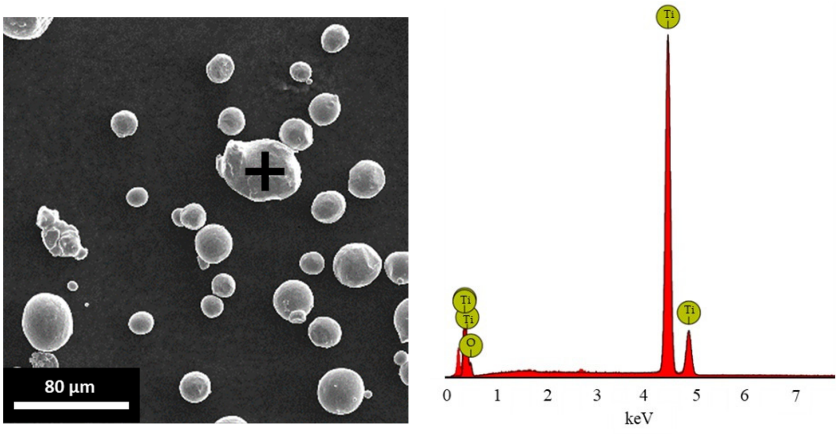

(**a**) (**b**)

Figure 1. Titanium particles morphology (**a**); EDS spectrum of the analysis carried out on the marked particle (**b**).

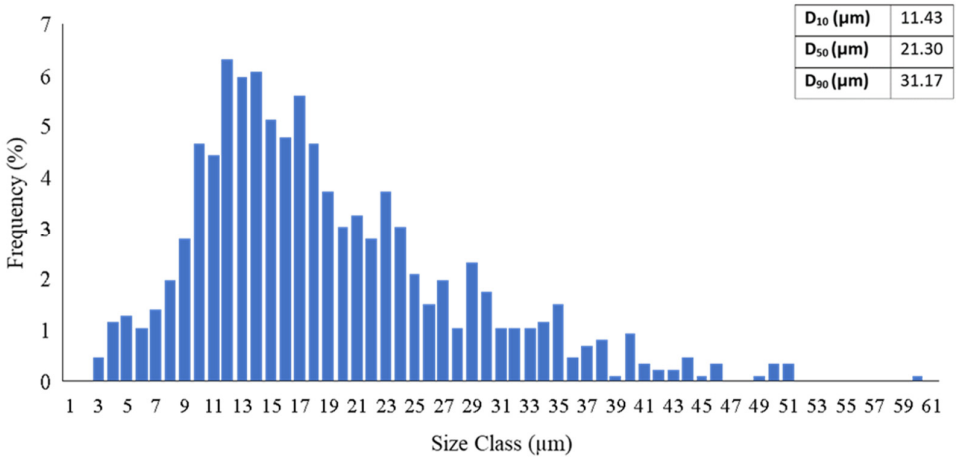

Figure 2. Particle size distribution of CP-Ti gr. 2 powder.

The measured values of powder flowability, apparent density, and tap density and the calculated values of the Hausner Ratio (HR) and Compressibility Index (CI) are shown in Table 3.

Table 3. Results of flowability tests.

Flowability	
Apparent Density (ρ_{app})	2.49 ± 0.01 g/cm^3
Tap Density (ρ_{tap})	2.85 ± 0.01 g/cm^3
Flowability (Hall test)	41.6 ± 0.9 s
Compressibility Index	13
Hausner Ratio	1.15

The Hausner Ratio and the Compressibility Index were calculated according to Equations (3) and (4), respectively. According to Carr's classification, the flowability of the powder was evaluated as good.

$$HR = \frac{\rho_{tap}}{\rho_{apparent}} \quad (3)$$

$$CI = 100 \cdot \frac{\rho_{tap} - \rho_{apparent}}{\rho_{apparent}} \quad (4)$$

The particle size and size distribution were consistent with those of the powders generally used for the L-PBF process. The particle spherical shape favored the good flowability found according to Carr's classification and then promoted the deposition of a homogeneous and rather compact powder bed.

A powder absorptivity value of 0.6 at the laser beam wavelength (1064 nm) was experimentally measured for the powders used for the L-PBF process. This result is consistent with the literature, which highlights that the absorptivity of a powder bed made of Cp titanium is affected by several factors. In fact, absorptivity has been shown to vary in the range of 0.5–0.8, depending on the porosity and the penetration depth of the laser beam, as it increases with the penetration depth and decreases with an increasing porosity [48]. Additionally, an oxide layer formed on the surface of aged titanium promotes multiple reflections of the radiation, which, in turn, causes the reduced penetration of the radiation and results in a loss of absorptivity [49]. Consistent with this, Zhou Y.H. et al. [44] calculated an absorptivity of 0.63 for Ti particles contaminated with a surface oxide layer. The presence of alloying elements and impurities can also significantly affect the laser absorptivity during LPBF; for instance, a laser absorptivity of only 0.3 was reported for Ti-6Al-4V powder [44,50].

In this paper, the absorptivity value of 0.6 is adopted for calculations.

3.2. Volumetric Energy Density (VED) and Efficient VED (VED_{eff}) Calculation

The energy that the laser beam delivers to 1 mm^3 of the powder bed (VED) was calculated according to Equation (1), where t = 30 μm, and h = 80 μm; P and v ranged between 90 and 140 W and between 221 and 1167 mm/s, respectively.

The efficient volumetric energy density (VED_{eff}), which represents the energy that is actually available for processing 1 mm^3 of the powder bed, was calculated according to Equation (2).

This modified approach considers that not all the energy is effectively acquired by the powder bed since a part of it is not absorbed by the powder and another part is dispersed in the environment because of thermal conduction phenomena. A laser with a spot size of 0.1 mm was always used. The 0.6 value of absorptivity (β), measured for the titanium powder, was adopted for VED_{eff} calculation. According to Ferro et al. [37], the value of thermal diffusivity (α) of a solid metallic material at room temperature can be used for calculation. A value of 8 mm^2/s was measured for solid Cp grade 1 Ti at room temperature by Slezak et al. [51]. On the other hand, the thermal diffusivity of solid pure titanium changes in a complex manner with an increase in temperature. It was found to decrease to 6 mm^2/s with a temperature increase up to 500 °C, to maintain this value in the range of 500–800 °C, and then to increase again progressively up to 8 mm^2/s in the temperature range of 800–1000 °C, with this α value remaining constant up to 1400 °C [51]. In addition, the thermal diffusivity of pure titanium at its melting temperature (1668 °C) was calculated to be 9.5 mm^2/s [52]. Therefore, an alternative value of α can be calculated by averaging the mean value of α in the temperature range below the melting point and the α value of the liquid titanium. A rough value of 8.5 mm^2/s, not very different from that of solid titanium at room temperature, can be obtained in this way. Moreover, it is also important to consider the thermal diffusivity of the molten titanium since the interaction between the laser beam and the powder bed lasts a small fraction of a second and then the liquid titanium forms almost immediately. Other possible approaches for defining the thermal diffusivity value are hard to establish because the thermal diffusivity of the powder bed during L-PBF was found to depend not only on the temperature but on the processing parameters, too [53]. On the basis of these considerations, in this paper, both the thermal diffusivity values of 8 mm^2/s and 8.5 mm^2/s are used for the VED_{eff} calculation.

3.3. Thermodynamical Work Window Assessment

The calculation of the boundaries of the thermodynamical work window was aimed at defining the range of energy that the unit of volume of the powder layer should acquire during the AM process. This energy should be compared with the energy delivered by the laser source to 1 mm^3 of powder (VED) or with the energy that 1 mm^3 of powder can roughly use for heating and melting (VED_{eff}). As a matter of fact, VED_{eff} is significantly lower than VED owing to the reflectivity of the powder bed and the ratio between the heat dissipated by thermal conductivity and the heat stored inside the material (thermal diffusivity). The amount of energy suitable for the L-PBF process should be calculated by using thermodynamic data for titanium, such as the specific heat, enthalpy of fusion, and enthalpy of vaporization. These data can easily be found in the literature, but they refer to a mole or a mass unit of titanium. Conversion from moles to units of mass can be simply accomplished by using the titanium molar weight (47.9 g/mol). The thermodynamic data should then refer to 1 mm^3 of power bed to make a comparison with the volumetric energy densities. For this purpose, the tap density (ρ_{tap}) of the titanium powder (2.86×10^{-3} g/mm^3) was used because every very thin layer deposited during the L-PBF process is flattened by the recoater. The mechanical action of the recoater likely causes some powder compaction, which enhances the bed density over the apparent density of the powder. The energy required to heat the powder from 25 °C to the melting temperature (1668 °C) was calculated according to Equation (5) by using the average value of the

specific heat (C_{sp}) of titanium in this temperature range (30.57 J/mol K, 0.64 J/g K) [54] and considering that one mm^3 of Ti powder contains 2.86×10^{-3} g of metal.

$$Q_{Heat} = \Delta T \cdot C_{sp} \cdot \rho_{tap} = (1668 - 25) \cdot 0.64 \cdot 2.86 \cdot 10^{-3} = 3.01\ \mathrm{J/mm^3} \quad (5)$$

A value of enthalpy of fusion (H_{fus}) of 436.4 J/g [55] was adopted to evaluate the energy required to melt the titanium powder (Equation (6)).

$$Q_{Fus} = H_{fus} \cdot \rho_{tap} = 436.4 \cdot 2.86 \cdot 10^{-3} = 1.25\ \mathrm{J/mm^3} \quad (6)$$

The sum of these values (4.26 J/mm^3) in principle represents the amount of energy that is sufficient to melt 1 mm^3 of powder bed, but it might not be enough to grant strong bonds between the current irradiated layer and the one previously deposited. In fact, to achieve this result, the heat should reach the previous layer, causing welding between the layers owing to diffusion and melting. The depth penetration of the laser beam depends on several processing parameters: the laser power, laser beam diameter, etching distance, layer thickness, and scanning speed. Nonetheless, the value of 4.26 J/mm^3 represents a low limit of energy that should be exceeded during manufacturing by L-PBF. Conversely, too much energy could cause the evaporation of molten titanium, with the formation of porosity inside the manufactured part. The evaporation enthalpy (H_{ev}) of titanium is 8955 J/g [55] and therefore the energy required for the evaporation of the unit of volume of powder is calculated as follows (Equation (7)):

$$Q_{Ev} = H_{ev} \cdot \rho_{tap} = 8955 \cdot 2.86 \cdot 10^{-3} = 25.61\ \mathrm{J/_{mm^3}} \quad (7)$$

The upper limit of the thermodynamical work window (29.87 J/mm^3) can be established by adding this evaporation heat to the lower limit.

3.4. Optimization of the Processing Parameters by Using VED, VED_{eff} and Thermodynamical Work Window

The volumetric energy densities (VED and VED_{eff}) selected to run the L-PBF jobs are shown in Table 4. The laser power and the laser speed combinations tested in these forty-two experiments are also reported in this table with the resulting porosity of the specimens. Porosity was taken as an index of the effectiveness of the processing parameters, with the aim of optimizing the experimental conditions for powder bed fusion. It is remarkable that different porosity levels can be achieved by using different combinations of power and scanning speed even though all these couples of parameters correspond to the same VED value. Differences in porosity of up to 50% could be observed for the samples processed using the same energy density (Figure 3), but a relation between porosity and the variation of power or scanning speed could not be clearly established. This means that not only the amount of energy provided by the laser but also the way it is delivered (a combination of power and scanning speed) affects the porosity. However, the relation between power, scanning speed, and porosity is complex; for instance, curves of porosity against scanning speed were found to show different trends depending on the laser power in the case of the L-PBF of Ti-6Al-4V [15]. The range of measured porosity values became narrower starting from VED values of 90 J/mm^3 and then the porosity progressively approached 1% with a VED increase (Figure 3). Table 4 shows that the VED values that granted good sample densification in our investigation were well over the thermodynamical work window established by using thermodynamic data. In fact, the volumetric energy density of 110 J/mm^3, granting a porosity below 2%, was about 28.5 times greater than the lower limit of the thermodynamical work window and 3.7 times greater than the upper limit. This means that optimized values of VED can only be established by using a trial-and-error approach while an optimized VED value cannot be forecasted.

Table 4. Processing parameter, sample porosity, VED, and VED_{eff} (* calculated with α = 8 mm^2/s; ** calculated with α = 8.5 mm^2/s).

Sample	Laser Power (W)	Scanning Speeds (mm/s)	Porosity (%)	VED (J/mm^3)	VED $*_{eff}$ (J/mm^3)	VED $**_{eff}$ (J/mm^3)
1	90	536	9.62	35	11.52	11.19
2	100	595	8.24		12.15	11.80
3	110	655	8.96		12.73	12.36
4	120	714	12.97		13.30	12.92
5	130	774	12.82		13.84	13.44
6	140	833	10.45		14.37	13.96
7	90	750	5.56	50	13.77	13.38
8	100	833	7.26		14.52	14.10
9	110	917	5.51		15.22	14.78
10	120	1000	5.23		15.90	15.44
11	130	1083	5.50		16.55	16.08
12	140	1167	6.65		17.17	16.68
13	90	536	7.47	70	16.29	15.82
14	100	595	6.03		17.18	16.68
15	110	655	6.26		18.01	17.49
16	120	714	6.61		18.82	18.28
17	130	774	6.06		19.58	19.02
18	140	833	5.34		20.32	19.74
19	90	417	1.95	90	18.47	17.93
20	100	463	1.81		19.47	18.91
21	110	509	1.63		20.43	19.84
22	120	556	2.88		21.32	20.71
23	130	602	1.83		22.20	21.56
24	140	648	2.12		23.04	22.38
25	90	341	1.77	110	20.42	19.84
26	100	379	1.67		21.52	20.91
27	110	417	1.52		22.57	21.92
28	120	455	1.88		23.57	22.90
29	130	492	1.63		24.56	23.85
30	140	530	1.80		25.48	24.75
31	90	288	1.16	130	22.22	21.58
32	100	321	1.13		23.39	22.72
33	110	353	1.29		24.53	23.83
34	120	385	1.48		25.62	24.89
35	130	417	0.98		26.67	25.91
36	140	449	1.25		27.68	26.89
37	90	221	1.11	150	25.37	24.64
38	100	245	1.12		26.77	26.00
39	110	270	1.02		28.05	27.25
40	120	294	1.26		29.32	28.48
41	130	319	0.93		30.49	29.62
42	140	343	1.03		31.67	30.78

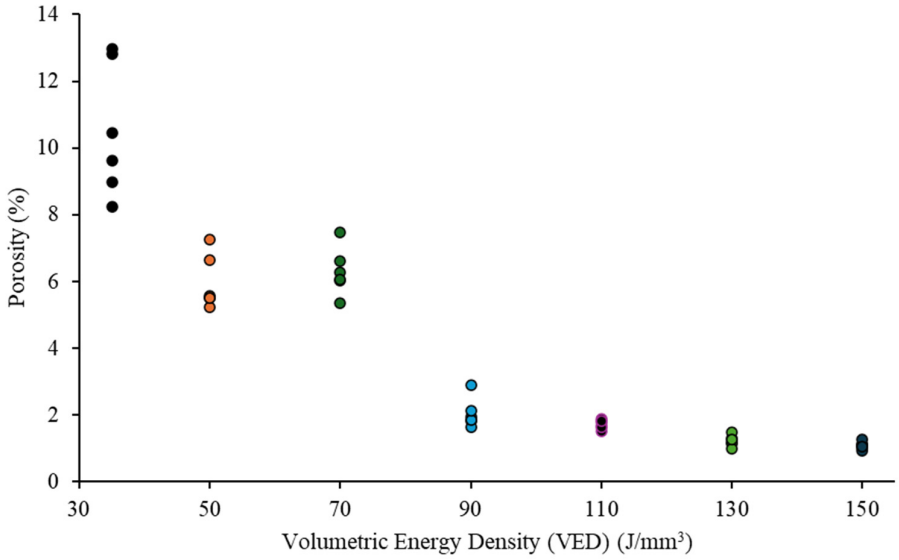

Figure 3. VED values against related porosity values.

The plot of porosity against the efficient energy density also shows a significant scattering of porosity values when VED_{eff} is lower than 20 J/mm^3 (Figure 4). In fact, in this case, samples manufactured using similar VED_{eff} values showed different porosity levels depending on the different combinations of the processing parameters adopted. In the range of energy density between 17.5 J/mm^3 and 20 J/mm^3, the porosity seemed mainly to be affected by the scanning speed since porosity generally increased with a scanning speed increase (Table 2). When the efficient energy density exceeded 20 J/mm^3, the porosity quickly decreased towards 1% or less. As seen in this region of Figure 4, a variation in energy density only causes small porosity changes. However, a clear trend can be appreciated as porosity progressively decreases with the VED_{eff} increase. Almost all the experimental conditions tested were consistent with the calculated work windows; only two samples out of the forty-two were processed using an efficient energy density slightly exceeding the upper limit of the thermodynamical work window (about 30 J/mm^3). Nevertheless, these process conditions were not detrimental for the sample densification. However, there was a clear correlation between the VED_{eff} and the thermodynamic work window since a good densification could always be achieved by using efficient volumetric energy densities at least equal to 70% of the upper limit value of the work window. To conclude, the calculation of the thermodynamical work window starting from thermodynamic data can be used to optimize the processing parameters, which should be coherent with an efficient energy density near the upper limit of this window.

The characteristics of the microstructures of the specimens were consistent with the porosity measurements (Figures 5 and 6). Important porosity could be observed in the samples printed using low values of energy density (VED up to 70 J/mm^3 and VED_{eff} up to 20 J/mm^3). These pores were rather large and showed an irregular shape, which is characteristic of defects caused by an insufficient delivery of energy to the sample and therefore by a lack of fusion [15,56] (Figure 5a,b,g). These kinds of defects could also be occasionally observed in samples printed by using VED of 90 J/mm^3 and VED_{eff} up to 20.43 J/mm^3 (Figure 5c,h). Inside these voids, spherical particles of unmolten titanium could be clearly distinguished (Figure 5g,h). Under these experimental conditions, a residual porosity just below 2% was detected. A further increase in the energy delivered resulted in a decrease in porosity and a modification of the pore shape. In this last case, small voids with a spherical shape could be observed (Figure 5d–f). This defect morphology could be due to the entrapment of gaseous species in the melting pool during solidification [56,57]. This porosity could be ascribed to moisture and/or internal porosity present in titanium particles used for the additive manufacturing process. Nonetheless, these kinds of defects

observed in the present work did not seem to be consistent with a possible vaporization of molten titanium, which, in principle, could occur when the upper limit of the thermodynamical work window was crossed. In fact, the measured porosity did not increase when VED_{eff} slightly exceeded this theoretical upper limit (sample 42 in Table 4) and the samples processed under conditions approaching the upper limit of the thermodynamical work window showed low porosity and fine microstructures (Figure 5f). Chemical etching highlighted the morphology and the orientation of the crystal grains (Figure 6). Elongated grains grown along the z direction could be observed under all the processing conditions. The temperature gradient inside the melting pools and the resulting solidification direction caused a grain growth almost parallel to the building direction. However, this microstructure characterized by elongated grains could be modified by thermal treatments, which currently are carried out after LPBF mainly with the aim of relaxing the residual stresses that arise during rapid cooling under severe thermal gradients. Large pores caused locally by a lack of fusion were present in the microstructure of the sample processed using lower energy while only small spherical pores could be found in the sample processed by using higher energy density (Figure 6).

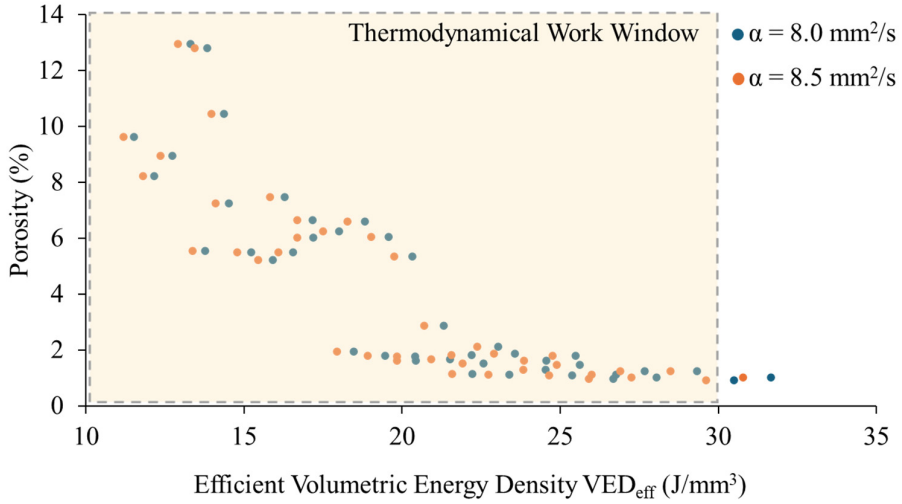

Figure 4. Porosity versus efficient volumetric energy density—blue dots: VED_{eff} calculated with $\alpha = 8\ mm^2/s$; red dots: VED_{eff} calculated with $\alpha = 8.5\ mm^2/s$.

The microhardness values are summarized in Figure 7 with their standard deviations. These results are fully consistent with the outcomes of the microstructure characterization. The microhardness progressively increased with the residual porosity decrease and almost constant Vickers hardness values (between 257.4 ± 7.6 HV and 278.1 ± 9.1 HV) could be observed for the samples processed under optimized conditions. In fact, this result was achieved when using values of efficient volumetric energy density over 20 J/mm^3, which granted a residual porosity around 1%. The samples with higher porosity levels showed lower hardness and a rather wide scattering of hardness values as highlighted by the standard deviation bars. Even though the indentations were performed quite far from the defects visible on the surface, it is very likely that pores randomly distributed below this surface affected the hardness measurement and caused the scattering of the results. The measured microhardness values were consistent (only slightly higher) with those reported in the literature (247–250 ± 19 HV) for Cp Ti processed by L-PBF and not submitted to a post-processing thermal treatment [57]. As a matter of fact, the hardness of the samples processed by L-PBF was higher than that resulting from traditional processing methods owing to the finer microstructure achieved during the L-PBF process, driven by a steep thermal gradient and rapid thermal cycles. In fact, a Vickers microhardness of 200 ± 5 only has been reported for Cp Ti items produced by casting and not submitted to final thermal treatments; however, the microhardness can be significantly enhanced by a tailored thermal treatment of annealing and ageing up to 260 ± 23 [58].

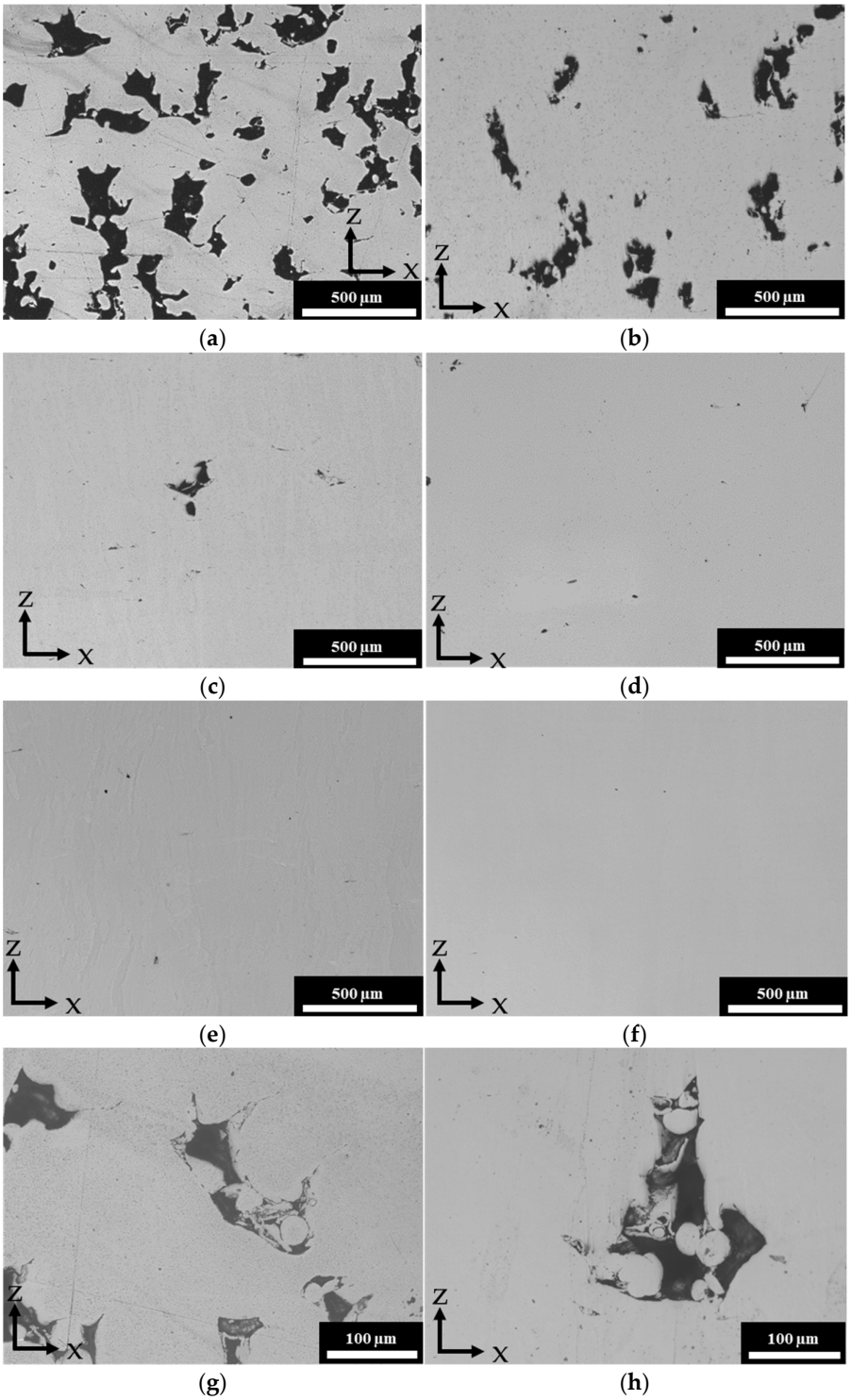

Figure 5. Defects in L-PBF of Ti processed with power of 110 W and different scanning speeds. All the micrographs were acquired on the X-Z cross-section (parallel to the building direction)—(**a**): v = 917 mm/s, VED 50, VED*$_{eff}$ 15.22, and VED**$_{eff}$ 14.78; (**g**): detail of "(**a**)" showing lack of fusion; (**b**): v = 655 mm/s, VED 70, VED*$_{eff}$ 18.01, and VED**$_{eff}$ 17.49; (**c**): v = 509 mm/s, VED 90, VED*$_{eff}$ 20.43, and VED**$_{eff}$ 19.84; (**h**): detail of "(**c**)" showing lack of fusion; (**d**): v = 417 mm/s, VED 110, VED*$_{eff}$ 22.57, and VED**$_{eff}$ 21.92; (**e**): v = 353 mm/s, VED 130, VED*$_{eff}$ 24.53, and VED**$_{eff}$ 23.83; (**f**): v = 270 mm/s, VED 150, VED*$_{eff}$ 28.05, and VED**$_{eff}$ 27.25.

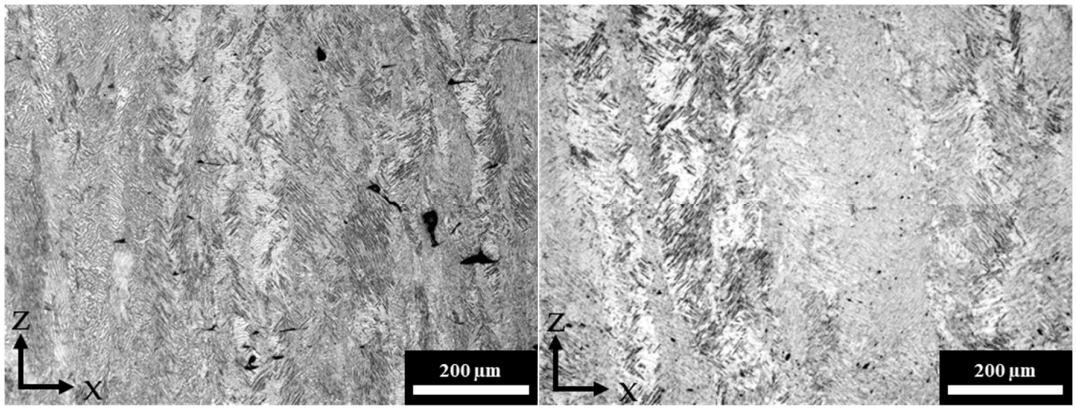

Figure 6. Micrographs of the etched cross-section, acquired on the X-Z cross-section (parallel to the building direction): (**a**) P = 110 W, v = 509 mm/s, VED 90, and VED*eff 20.42 J/mm^3; (**b**) P = 110 W, v = 270 mm/s, VED 150, and VED*eff 28.05 J/mm^3.

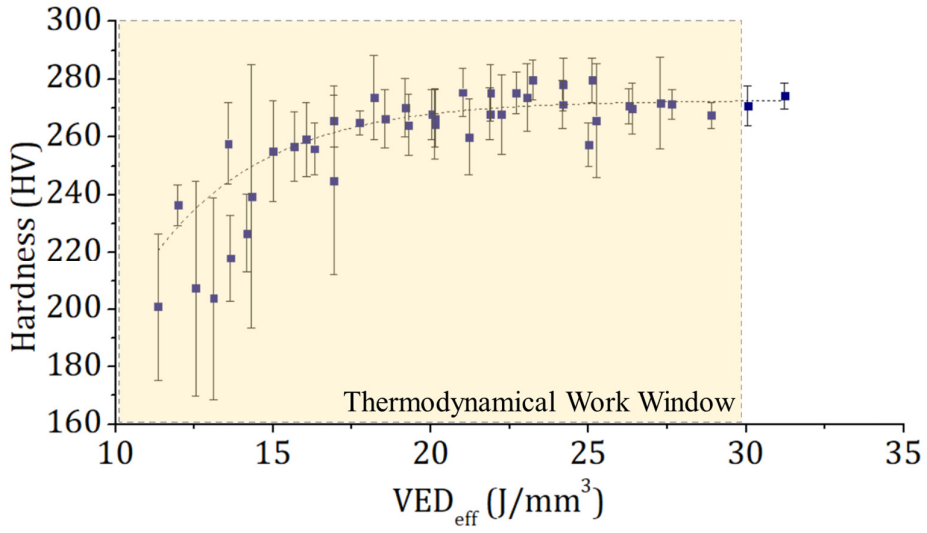

Figure 7. Vickers microhardness versus mean value of VED_{eff} adopted for L-PBF (average between VED^*_{eff} and VED^{**}_{eff}).

4. Conclusions

The effectiveness of a non-conventional approach for the optimization of processing parameters adopted in the L-PBF process of commercially pure titanium powder was successfully tested. This approach, which is based on the use of the so-called Efficient Volumetric Energy Density (VED_{eff}), was previously reported in the literature for the printing of the AlSi10Mg alloy and Maraging steel 300, but had never been tested for titanium powders. The VED_{eff} can be calculated using process parameters (laser power, scanning speed, hatching distance, and laser spot diameter) combined with material and powder properties, such as absorptivity and thermal diffusivity. The absorptivity and thermal diffusivity values can easily be experimentally measured or found in the literature. The VED_{eff} roughly represents the amount of energy that is effectively available for the process. In fact, a portion of the energy delivered by the laser source is either reflected or dissipated in the environment due to thermal conduction. For this reason, it is impossible to determine appropriate processing parameters merely based on the Volumetric Energy Density (VED) that the laser source delivers to the powder.

On the contrary, appropriate levels of efficient energy can be defined by comparison with the thermodynamical work window. This work window ranges between the minimum energy necessary to heat and melt the powder and the maximum amount of energy that can

be absorbed by the powder without causing vaporization. The lower and upper limits of the work window can be readily calculated starting from the thermodynamic data reported in the literature. In this manner, possible combinations of the processing parameters can be selected before carrying out experimental printing jobs. This approach represents a convenient alternative to the trial-and-error method (based on testing, experimentally, several parameter combinations or VED values) as it limits both costs and the time spent finding appropriate processing parameters. In fact, the selection of a set of processing parameters can be accomplished on the basis of the calculation of the work window and the choice of a VED_{eff} consistent with this energy range. This method could be adopted for many kinds of metallic materials, provided that the values of their absorptivity, diffusivity, specific heat, heat of fusion and vaporization are available.

The results of our investigation showed that many parameter combinations and the relevant efficient energy values, consistent with the thermodynamical work window, are suitable for the L-PBF process of CP-Ti gr. 2. Additionally, several combinations of power and scanning speed adopted in this work gave rise to very similar values of efficient volumetric energy density and subsequently resulted in similar microstructures and mechanical features in the printed samples. However, the range of the most appropriate energy density values should be further restricted relative to the thermodynamical work window to decrease the residual porosity to around 1% and achieve the best mechanical features. Several defects caused by lack of fusion were observed when adopting efficient energy values corresponding to the lower half of the thermodynamical work window. In fact, the energy acquired by the powder bed must be sufficient not only for heating and melting it but also to ensure welding both between adjacent laser tracks as well as between layers.

Every parameter combination resulting in an efficient energy density corresponding to the upper third part of the thermodynamical work window gave satisfactory results in terms of density, microstructure, and hardness. In conclusion, the approach used in this work proved to be a sort of rule of thumb that can successfully guide the process parameter optimization for the L-PBF of titanium. Moreover, it can be easily exploited for selecting proper processing parameters for industrial applications, as well as for research purposes.

Author Contributions: Conceptualization, C.F.B. and E.P.; methodology, C.F.B., T.S., M.R. and E.P.; validation, C.F.B., T.S., M.R. and E.P.; investigation, T.S. and M.R.; data curation, C.F.B., T.S. and M.R.; writing—original draft preparation, C.F.B.; writing—review and editing, C.F.B., T.S., M.R. and E.P.; visualization, T.S. and M.R.; supervision, C.F.B. and E.P. All authors have read and agreed to the published version of the manuscript.

Funding: This research received no external funding.

Data Availability Statement: The original contributions presented in this study are included in the article. Further inquiries can be directed to the corresponding author.

Conflicts of Interest: The authors declare no conflicts of interest.

References

1. Ladani, L.; Sadeghilaridjani, M. Review of Powder Bed Fusion Additive Manufacturing for Metals. *Metals* **2021**, *11*, 1391. [CrossRef]
2. Dejene, N.D.; Lemu, H.G. Current Status and Challenges of Powder Bed Fusion-Based Metal Additive Manufacturing: Liter-ature Review. *Metals* **2023**, *13*, 424. [CrossRef]
3. Sarzyński, B.; Śnieżek, L.; Grzelak, K. Metal Additive Manufacturing (MAM) Applications in Production of Vehicle Parts and Components—A Review. *Metals* **2024**, *14*, 195. [CrossRef]
4. Shanthar, R.; Chen, K.; Abeykoon, C. Powder-Based Additive Manufacturing: A Critical Review of Materials, Methods, Opportunities, and Challenges. *Adv. Eng. Mater.* **2023**, *25*, 2300375. [CrossRef]
5. Yao, L.; Ramesh, A.; Xiao, Z.; Chen, Y.; Zhuang, Q. Multimetal Research in Powder Bed Fusion: A Review. *Materials* **2023**, *16*, 4287. [CrossRef] [PubMed]
6. Qi, X.; Liang, X.; Wang, J.; Zhang, H.; Wang, X.; Liu, Z. Microstructure tailoring in laser powder bed fusion (L-PBF): Strategies, challenges, and future outlooks. *J. Alloys Compd.* **2024**, *970*, 172564. [CrossRef]

7. Zong, H.; Kang, N.; Qin, Z.; El Mansori, M. A review on the multi-scaled structures and mechanical/thermal properties of tool steels fabricated by laser powder bed fusion additive manufacturing. *Int. J. Miner. Met. Mater.* **2024**, *31*, 1048–1071. [CrossRef]
8. Zhang, H.; Hou, Y.; Wang, X.; Li, X.; He, Y.; Li, F.; Lu, Y.; Su, H. High throughput in-situ synthesis of Fe-Cr-Ni alloys via laser powder bed fusion: Exploring the microstructure and property evolution. *Addit. Manuf.* **2024**, *81*, 103996. [CrossRef]
9. Li, K.; Yang, T.; Gong, N.; Wu, J.; Wu, X.; Zhang, D.Z.; Murr, L.E. Additive manufacturing of ultra-high strength steels: A review. *J. Alloys Compd.* **2023**, *965*, 171390. [CrossRef]
10. Wang, X.; Zhang, D.; Li, A.; Yi, D.; Li, T. A Review on Traditional Processes and Laser Powder Bed Fusion of Aluminum Alloy Microstructures, Mechanical Properties, Costs, and Applications. *Materials* **2024**, *17*, 2553. [CrossRef] [PubMed]
11. Manjhi, S.K.; Sekar, P.; Bontha, S.; Balan, A.S.S. Additive manufacturing of magnesium alloys: Characterization and post-processing. *Int. J. Light. Mater. Manuf.* **2024**, *7*, 184–213. [CrossRef]
12. Peng, B.; Xu, H.; Song, F.; Wen, P.; Tian, Y.; Zheng, Y. Additive manufacturing of porous magnesium alloys for biodegradable orthopedic implants: Process, design, and modification. *J. Mater. Sci. Technol.* **2024**, *182*, 79–110. [CrossRef]
13. Adomako, N.K.; Haghdadi, N.; Primig, S. Electron and laser-based additive manufacturing of Ni-based superalloys: A review of heterogeneities in microstructure and mechanical properties. *Mater. Des.* **2022**, *223*, 111245. [CrossRef]
14. Volpato, G.M.; Tetzlaff, U.; Fredel, M.C. A Comprehensive Literature Review on Laser Powder Bed Fusion of Inconel Super-alloys. *Addit. Manuf.* **2022**, *55*, 102871.
15. Villa, R.; Liu, Y.; Siddique, Z. Review of defects and their sources in as-built Ti6Al4V manufactured via powder bed fusion. *Int. J. Adv. Manuf. Technol.* **2024**, *132*, 4105–4134. [CrossRef]
16. Luo, X.; Yang, C.; Li, D.; Zhang, L.C. Laser Powder Bed Fusion of Beta-Type Titanium Alloys for Biomedical Application: A Review. *Acta Metall. Sin. (Engl. Lett.)* **2024**, *37*, 17–28. [CrossRef]
17. Karimi, P.; Keshavarz, M.K.; Sadeghi, E.; Habibnejad, M.; Vlasea, M. Interplay of process, microstructure, and mechanical performance in electron beam-powder bed fusion of Ti48Al2Nb2Cr. *Addit. Manuf.* **2023**, *77*, 103811. [CrossRef]
18. Tyagi, S.A.; Manjaiah, M. Additive manufacturing of titanium-based lattice structures for medical applications—A review. *Bioprinting* **2023**, *30*, e00267. [CrossRef]
19. Depboylu, F.N.; Yasa, E.; Poyraz, Ö.; Minguella-Canela, J.; Korkusuz, F.; De los Santos López, M.A. Titanium based bone implants production using laser powder bed fusion technology. *J. Mater. Res. Technol.* **2022**, *17*, 1408–1426. [CrossRef]
20. Bartolomeu, F.; Gasik, M.; Silva, F.S.; Miranda, G. Mechanical Properties of Ti6Al4V Fabricated by Laser Powder Bed Fusion: A Review Focused on the Processing and Microstructural Parameters Influence on the Final Properties. *Metals* **2022**, *12*, 986. [CrossRef]
21. Tang, X.; Chen, X.; Sun, F.; Liu, P.; Zhou, H.; Fu, S. The current state of CuCrZr and CuCrNb alloys manufactured by additive manufacturing: A review. *Mater. Des.* **2022**, *224*, 111419. [CrossRef]
22. Howard, L.; Parker, G.D.; Yu, X.Y. Progress and Challenges of Additive Manufacturing of Tungsten and Alloys as Plas-ma-Facing Materials. *Materials* **2024**, *17*, 2104. [CrossRef] [PubMed]
23. Yang, Z.; Zhu, J.; Lu, B.; Liu, Y.; Shi, W.; Liu, M.; Wang, G.; Yan, X. Powder bed fusion pure tantalum and tantalum alloys: From original materials, process, performance to applications. *Opt. Laser Technol.* **2024**, *177*, 111057. [CrossRef]
24. Chen, Y.; Xiong, C.; Li, Y. Additive Manufacturing of Rare Earth Permanent Magnetic Materials: Research Status and Prospects. *Metals* **2024**, *14*, 446. [CrossRef]
25. Abedi, M.; Moskovskikh, D.; Romanovski, V.; Ozherelkov, D.; Gromov, A. Unlocking the potential of graphene-reinforced AlSi10Mg nanocomposites in laser powder bed fusion: A comprehensive review. *J. Alloys Compd.* **2024**, *978*, 173441. [CrossRef]
26. Kim, M.K.; Fang, Y.; Kim, J.; Kim, T.; Zhang, Y.; Jeong, W.; Suhr, J. Strategies and Outlook on Metal Matrix Composites Pro-duced Using Laser Powder Bed Fusion: A Review. *Metals* **2023**, *13*, 1658. [CrossRef]
27. Essien, U.; Vaudreuil, S. Issues in Metal Matrix Composites Fabricated by Laser Powder Bed Fusion Technique: A Review. *Adv. Eng. Mater.* **2022**, *24*, 2200055. [CrossRef]
28. Yang, G.; Xie, Y.; Zhao, S.; Qin, L.; Wang, X.; Wu, B. Quality Control: Internal Defects Formation Mechanism of Selective Laser Melting Based on Laser-powder-melt Pool Interaction: A Review. *Chin. J. Mech. Eng. Addit. Manuf. Front.* **2022**, *1*, 100037. [CrossRef]
29. Luo, Z.; Zhao, Y. A survey of finite element analysis of temperature and thermal stress fields in powder bed fusion Additive Manufacturing. *Addit. Manuf.* **2018**, *21*, 318–332. [CrossRef]
30. Shen, T.; Li, B. An integrated computation framework for predicting mechanical performance of single-phase alloys manufactured using laser powder bed fusion: A case study of CoCrFeMnNi high-entropy alloy. *Mater. Today Commun.* **2024**, *39*, 109180. [CrossRef]
31. Wang, P.; Yang, Y.; Moghaddam, N.S. Process modeling in laser powder bed fusion towards defect detection and quality control via machine learning: The state-of-the-art and research challenges. *J. Manuf. Process.* **2022**, *73*, 961–984. [CrossRef]
32. Phadke, N.; Raj, R.; Srivastava, A.K.; Dwivedi, S.; Dixit, A.R. Modeling and parametric optimization of laser powder bed fusion 3D printing technique using artificial neural network for enhancing dimensional accuracy. *Mater. Today Proc.* **2022**, *56*, 873–878. [CrossRef]
33. Babakan, A.M.; Davoodi, M.; Shafaie, M.; Sarparast, M.; Zhang, H. Predictive modeling of porosity in AlSi10Mg alloy fabricated by laser powder bed fusion: A comparative study with RSM, ANN, FL, and ANFIS. *Int. J. Adv. Manuf. Technol.* **2023**, *129*, 1097–1108. [CrossRef]

34. Noh, J.; Lee, J.; Seo, Y.; Hong, S.; Kwon, Y.-S.; Kim, D. Dimensionless parameters to define process windows of selective laser melting process to fabricate three-dimensional metal structures. *Opt. Laser Technol.* **2022**, *149*, 107880. [CrossRef]
35. Islam, Z.; Kunkel, W.; Hatler, C.; Thoma, D.J. Process optimization and scaling of molybdenum and tungsten in additive manufacturing techniques. *Int. J. Refract. Met. Hard Mater.* **2024**, *121*, 106689. [CrossRef]
36. Rankouhi, B.; Agrawal, A.K.; Pfefferkorn, F.E.; Thoma, D.J. A dimensionless number for predicting universal processing parameter boundaries in metal powder bed additive manufacturing. *Manuf. Lett.* **2021**, *27*, 13–17. [CrossRef]
37. Ferro, P.; Meneghello, R.; Savio, G.; Berto, F. A modified volumetric energy density–based approach for porosity assessment in additive manufacturing process design. *Int. J. Adv. Manuf. Technol.* **2020**, *110*, 1911–1921. [CrossRef]
38. Fischer, R.D.; Harvill, G.C.; Zhao, R.; Talebinezhad, H.; Prorok, B.C. A roadmap for tailoring the microstructure and mechanical properties of additively manufactured commercially-pure titanium. *Mater. Sci. Eng. A* **2024**, *892*, 146088. [CrossRef]
39. Depboylu, F.N.; Yasa, E.; Poyraz, O.; Korkusuz, F. Thin-Walled Commercially Pure Titanium Structures: Laser Powder Bed Fusion Process Parameter Optimization. *Machines* **2023**, *11*, 272. [CrossRef]
40. Zhang, J.; Liu, Y.; Bayat, M.; Tan, Q.; Yin, Y.; Fan, Z.; Liu, S.; Hattel, J.H.; Dargusch, M.; Zhang, M.-X. Achieving high ductility in a selectively laser melted commercial pure-titanium via in-situ grain refinement. *Scr. Mater.* **2021**, *191*, 155–160. [CrossRef]
41. Kovacı, H. Comparison of the microstructural, mechanical and wear properties of plasma oxidized Cp-Ti prepared by laser powder bed fusion additive manufacturing and forging processes. *Surf. Coat. Technol.* **2019**, *374*, 987–996. [CrossRef]
42. Traxel, K.D.; Bandyopadhyay, A. Influence of in situ ceramic reinforcement towards tailoring titanium matrix composites using laser-based additive manufacturing. *Addit. Manuf.* **2020**, *31*, 101004. [CrossRef] [PubMed]
43. Umeda, J.; Jia, L.; Chen, B.; Chen, K.; Li, S.; Shitara, K.; Kondoh, K. Precipitation and Distribution Behavior of In Situ-Formed TiB Whiskers in Ti64 Composites Fabricated by Selective Laser Melting. *Crystals* **2021**, *11*, 374. [CrossRef]
44. Zhou, Y.H.; Zhang, Z.H.; Wang, Y.P.; Liu, G.; Zhou, S.Y.; Li, Y.L.; Shen, J.; Yan, M. Selective laser melting of typical metallic materials: An effective process prediction model developed by energy absorption and consumption analysis. *Addit. Manuf.* **2019**, *25*, 204–217. [CrossRef]
45. *ASTM B213-20*; Standard Test Methods for Flow Rate of Metal Powders Using the Hall Flowmeter Funnel. ASTM International: West Conshohocken, PA, USA, 2020.
46. *ASTM B311-17*; Standard Test Method for Density of Powder Metallurgy (PM) Materials Containing Less Than Two Percent Porosity. ASTM International: New York, NY, USA, 2019.
47. *ISO 6507-1:2023*; Metallic Materials—Vickers Hardness Test—Part 1: Test Method. International Organization for Standardization: Ginerva, Switzerland, 2023.
48. Antony, K.; Rakeshnath, T.R. Study on selective laser melting of commercially pure titanium powder. *Proc. Inst. Mech. Eng. B J. Eng. Manuf.* **2019**, *233*, 1794–1807. [CrossRef]
49. Brandau, B.; Da Silva, A.; Wilsnack, C.; Brueckner, F.; Kaplan, A.F.H. Absorbance study of powder conditions for laser additive manufacturing. *Mater. Des.* **2022**, *216*, 110591. [CrossRef]
50. Cook, P.S.; Ritchie, D.J. Determining the laser absorptivity of Ti-6Al-4V during laser powder bed fusion by calibrated melt pool simulation. *Opt. Laser Technol.* **2023**, *162*, 109247. [CrossRef]
51. Slezak, T.; Zmywaczyk, J.; Koniorczyk, P. Thermal Diffusivity Investigations of the Titanium Grade 1 in Wide Tem-perature Range. In *AIP Conference Proceedings, Proceedings of the THERMOPHYSICS 2019: 24th International Meeting of Thermophysics and 20th Conference REFRA, Trnava, Slovakia, 22–24 October 2019*; American Institute of Physics Inc.: Melville, NY, USA, 2019; Volume 2170.
52. Zhou, K.; Wang, H.P.; Chang, J.; Wei, B. Experimental study of surface tension, specific heat and thermal diffusivity of liquid and solid titanium. *Chem. Phys. Lett.* **2015**, *639*, 105–108. [CrossRef]
53. Akwaboa, S.; Zeng, C.; Amoafo-Yeboah, N.; Ibekwe, S.; Mensah, P. Thermophysical Properties of Laser Powder Bed Fused Ti-6Al-4V and AlSi10Mg Alloys Made with Varying Laser Parameters. *Materials* **2023**, *16*, 4920. [CrossRef] [PubMed]
54. Chase, M.W., Jr. *NIST-JANAF Themochemical Tables*, 4th ed.; American Institute of Physics: College Park, MD, USA, 1998; Volume 9, pp. 1–1951.
55. Fischer, P.; Leber, H.; Romano, V.; Weber, H.P.; Karapatis, N.P.; André, C.; Glardon, R. Microstructure of near-infrared pulsed laser sintered titanium samples. *Appl. Phys. A Mater. Sci. Process.* **2004**, *78*, 1219–1227. [CrossRef]
56. Ghio, E.; Cerri, E. Additive Manufacturing of AlSi10Mg and Ti6Al4V Lightweight Alloys via Laser Powder Bed Fusion: A Review of Heat Treatments Effects. *Materials* **2022**, *15*, 2047. [CrossRef]
57. Wysocki, B.; Maj, P.; Krawczyńska, A.; Rożniatowski, K.; Zdunek, J.; Kurzydłowski, K.J.; Świeszkowski, W. Microstructure and mechanical properties investigation of CP titanium processed by selective laser melting (SLM). *J. Mater. Process. Technol.* **2017**, *241*, 13–23. [CrossRef]
58. Soares, S.; Rocha, D.; Adabo, G.L.; Elias, G.; Henriques, P.; Antônio, M.; Nóbilo, A. Vickers Hardness of Cast Commercially Pure Titanium and Ti-6Al-4V Alloy Submitted to Heat Treatments. *Braz. Dent. J.* **2006**, *17*, 126–129.